Monthly Notices of the ROYAL ASTRONOMICAL SOCIETY

MNRAS **527,** 1521–1533 (2024) https://doi.org/10.1093/mnras/stad3033
Advance Access publication 2023 October 05

Ultracool spectroscopic outliers in *Gaia* DR3

W. J. Cooper,[1,2]★ R. L. Smart,[2] H. R. A. Jones[1] and L. M. Sarro[3]

[1]*Centre for Astrophysics Research, University of Hertfordshire, Hatfield, Hertfordshire AL10 9AB, UK*
[2]*Istituto Nazionale di Astrofisica, Osservatorio Astrofisico di Torino, Strada Osservatorio 20, I-10025 Pino Torinese, Italy*
[3]*Departamento de Inteligencia Artificial, ETSI Informática, UNED, Juan del Rosal, E-16 28040 Madrid, Spain*

Accepted 2023 October 2. Received 2023 September 28; in original form 2023 July 24

ABSTRACT

Gaia DR3 provided a first release of RP spectra and astrophysical parameters for ultracool dwarfs (UCDs). We used these *Gaia* RP spectra and astrophysical parameters to select the most outlying UCDs. These objects have spectral types of M7 or later and might be young brown dwarfs or low-metallicity objects. This work aimed to find UCDs that have *Gaia* RP spectra significantly different to the typical population. However, the intrinsic faintness of these UCDs in *Gaia* means that their spectra were typically rather low signal-to-noise ratio in *Gaia* DR3. This study is intended as a proof of concept for future iterations of the *Gaia* data releases. Based on well-studied subdwarfs and young objects, we created a spectral type-specific color ratio, defined using *Gaia* RP spectra; this ratio is then used to determine which objects are outliers. We then used the objects kinematics and photometry external to *Gaia* to cut down the list of outliers into a list of 'prime candidates'. We produce a list of 58 *Gaia* RP spectra outliers, seven of which we deem as prime candidates. Of these, six are likely subdwarfs and one is a known young stellar object. Four of six subdwarf candidates were known as subdwarfs already. The two other subdwarf candidates, namely 2MASS J03405673 + 2633447 (sdM8.5) and 2MASS J01204397 + 6623543 (sdM9), are new classifications.

Key words: brown dwarfs – stars: kinematics and dynamics – stars: late-type.

1 INTRODUCTION

Ultracool dwarfs (UCDs) are objects with spectral types cooler than M7 ($T_{\rm eff}\lesssim$2700 K), consisting of late M, L, T, and Y dwarfs. These newest spectral types were first described by Kirkpatrick et al. (1999), Burgasser et al. (2002), and Cushing et al. (2011). Spectral types of UCDs are primarily driven by changes in effective temperature, while other features (e.g. low-surface gravity, low-metallicity) can further refine them (see Kirkpatrick 2005). The aim of this work is to use the Gaia data to select outlying UCDs and in particular, the youngest and oldest examples.

Subdwarfs are old objects, with lower metallicities than field objects. As such, multi-wavelength photometric cross-matches are an ideal method to select subdwarf candidates. Notably, optical surveys like *Gaia* (Gaia Collaboration et al. 2016) and Pan-STARRS (Chambers et al. 2016) are typically compared with near/mid-infrared surveys including 2MASS (Skrutskie et al. 2006) and AllWISE (Cutri et al. 2013). Kinematically, subdwarfs, due to their age, are much faster than field objects. Hence, subdwarfs (depending on their metallicity and age) are either thick disc or halo objects. Multiple literature sources discuss the selections and classifications of thick disc/halo dwarfs (e.g. work by Leggett 1992). For purely kinematic selections of halo objects, when metallicity information is not present, Nissen & Schuster (2010) utilized either a cut of $V_{\rm total}$ > 180 km s^{-1} (Venn et al. 2004) or $V_{\rm total}$ > 210 km s^{-1} (Schönrich & Binney 2009; Koppelman, Helmi & Veljanoski 2018, depending on the Galactic model used), where $V_{\rm total}$ is the total space velocity, $V_{\rm total} = \sqrt{U^2 + V^2 + W^2}$, and U, V, W are the velocities in the Galactic reference frame. Likewise, selection of thick disc objects varies from $V_{\rm total}$ > 85 km s^{-1} (Zhang & Zhao 2006) to $V_{\rm total}$ > 70 km s^{-1} (Nissen & Schuster 2010) and $V_{\rm total}$ > 50 km s^{-1} (Gaia Collaboration et al. 2023c). Without radial velocity (RV) information, tangential velocity, $V_{\rm tan}$, has been often used as it is highly indicative of thick disc/halo membership. Ultracool subdwarfs follow this same detection criteria (Gizis 1997; Gizis & Reid 1999). We follow previous work discovering ultracool subdwarfs (e.g. Zhang et al. 2017b; Zhang, Burgasser & Smith 2019), which has the benefit from the selection of subdwarfs using virtual observatory tools (Lodieu et al. 2012, 2017) and all-sky surveys (Lépine, Shara & Rich 2002a; Lépine 2008).

By comparison, young objects have typically lower surface gravities and are redder than field objects (Cruz et al. 2016). Unresolved binaries often occupy the same space on colour–absolute magnitude diagrams (CMDs) as young objects, hence purely photometric selections are contaminated (e.g. Marocco et al. 2017). Kinematically, young objects are slower than field objects, and are often still gravitationally bound to young moving groups (Gagné & Faherty 2018, and references therein). Gathering spectra of UCD candidates is therefore necessary for confirming youth, especially when the objects are isolated. The spectral confirmation of youth involves analyzing the surface gravity of the UCD, where a lower gravity indicates a younger object. Optical spectra are given Greek letter classifications with α as normal, β as intermediate, γ as low gravity (Cruz, Kirkpatrick & Burgasser 2009), and δ for extreme low gravity (Kirkpatrick et al. 2006).

★ E-mail: w.cooper@herts.ac.uk

Gaia is a European Space Agency mission launched in 2013 and in June 2022 released *Gaia* DR3 (Gaia Collaboration et al. 2023a) which, importantly for this work, included spectra. This is referred to as 'XP' spectra where 'X' can be interchanged with either 'B' or 'R' corresponding to the blue and red filters. *Gaia* provides five dimensional astrometric measurements (two positions, two proper motions, and parallax). *Gaia* also released RVs for objects with $G_{\mathrm{RVS}} \lessapprox 14$ mag (Katz et al. 2023), where G_{RVS} is the magnitude integrated across the *Gaia* RV spectrometer (RVS; Sartoretti et al. 2023). We focus here on RP spectra, which cover the far red optical regime from ≈600 to 1050 nm. The resolution of these internally calibrated spectra for UCDs are around 30–50 ($\Delta\lambda/\lambda$) (Montegriffo et al. 2023, who also discuss the external calibration).

Gaia is well suited to observe nearby early-type UCDs (see fig. 26, Gaia Collaboration et al. 2021, <L5, $d < 30$ pc). Known *Gaia* UCDs are documented in the *Gaia* Ultracool Dwarf Sample (GUCDS; Smart et al. 2017, 2019; Marocco et al. 2020, Cooper et al., submitted). GUCDS aims to be complete for known L dwarfs but also contains late-M dwarfs, T dwarfs and primary stars from any relevant common proper motion systems. Volume limited samples have been vital for understanding the UCD population, as performed by Gaia Collaboration et al. (2021), Kirkpatrick et al. (2021), and Reylé et al. (2021). We focus on late M to L dwarfs, for which the spectral features evolve as described by Tinney & Reid (1998) and Kirkpatrick et al. (1999). However, at the low resolution of *Gaia* RP spectra, individual features cannot be seen, leading to a merging of features (Sarro et al. 2023).

Recently, many discoveries have been using *Gaia* data with the focus of finding outlying objects and astrophysical parameters. For example, exploration of hot subdwarf stars in *Gaia* DR3 (Culpan et al. 2022) found 21 785 underluminous objects. Yao et al. (2023) uncovered 188 000 candidate metal-poor stars using *Gaia* XP spectra. Similarly, Andrae, Rix & Chandra (2023), following the study by Anders et al. (2023), applied `XGBoost` to determine metallicities for main-sequence dwarfs and giants. Parameters of stars, forward modelled from *Gaia* XP spectra, were also determined by Zhang, Green & Rix (2023).

In UCDs, spectral feature changes due to age or metallicity are not directly seen in the RP spectra, as the spectra are too low resolution to readily be isolated, they do however change the general shape of the RP spectra, most notably the centroids and intensity of the two to three peaks (Fig. 1 in this work and fig. 5 by Sarro et al. 2023). As effective temperature decreases in Fig. 1, the first peak (∼750 nm) disappears when approaching the stellar/substellar boundary (≈L3, Gaia Collaboration et al. 2021), whereas the second peak goes from being brighter than the third peak in M dwarfs, to being dimmer than the third peak in L dwarfs and being roughly equivalent in T dwarfs. In addition, the centroids of the peaks redshift with decreasing T_{eff}.

This work is focused on the characterization of the *Gaia* internally calibrated RP spectra and the isolation of young and subdwarf UCDs. Section 2 discusses the methodology, and the creation of a colour ratio; Section 3 presents the analysis and selection of prime candidates from external photometry and kinematics; Section 4 shows the results of our prime candidates; and Section 5 concludes and plans future work to counter the known issues.

2 METHOD

Here we discuss our iterative approach to deriving an outlier classifier. We started with the sample of UCDs in *Gaia* as discussed by Sarro et al. (2023). To summarize, the sample of *Gaia* UCDs consists of every object for which the ESP-UCD work package derived

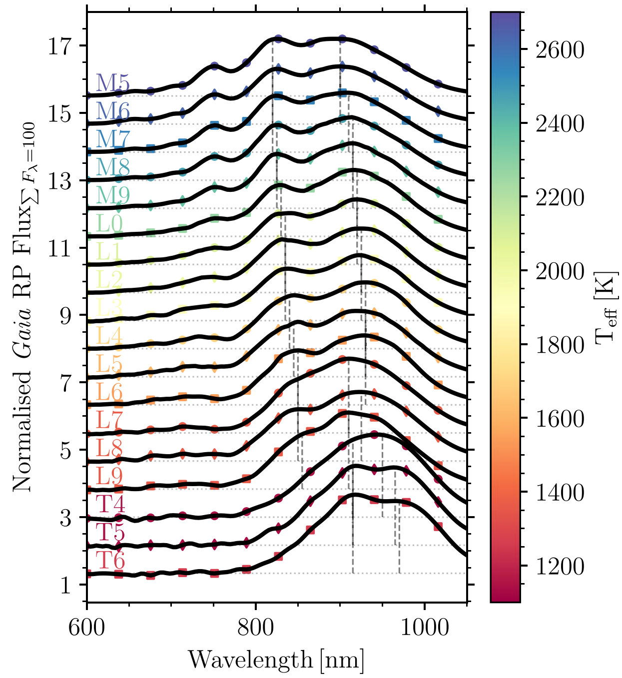

Figure 1. The normalized median RP fluxes for each spectral type (see Section 2.2) from M5 to T6. Each spectral type is indicated by the attached text with its corresponding median effective temperature given on the auxiliary axis. Vertical dashed lines are shown for every spectrum to indicate the position of the two primary spectral peaks. The normalized spectra were multiplied by a constant value such that the fluxes sum to 100 instead of 1 and are offset by a set value.

an effective temperature. The selection of UCDs from *Gaia* was as follows: $\varpi > 1.7$ mas, $G - G_{\mathrm{RP}} > 1$, $q_{33} > 60$, $q_{50} > 71$, $q_{67} > 83$ where q_{33}, q_{50}, and q_{67} are the 33.33, 50, and 66.67 percentiles of the total RP flux, respectively (Creevey et al. 2023). Of these 94 158 objects, only 21 205 have public RP spectra (see the online documentation and section 4 by De Angeli et al. 2023, for the *Gaia* spectra publication criteria). All effective temperatures discussed were from *Gaia* DR3, from the astrophysical parameters table and specific to the UCD work package ESP-UCD. The relevant columns originating from the ESP-UCD work package are `teff_espucd` and `flags_espucd`. One part of the *Gaia* DR3 RP spectra publication criteria, important for the search of spectral outliers, was that the *Gaia* RP UCD spectra were required to be one of the highest two quality flags (0–1, not 2 in `flags_espucd`). The flagging in ESP-UCD included measuring the Euclidean distance of a *Gaia* RP spectrum from its BT-Settl model counterpart. Whilst this requirement was vital for reducing the number of published *Gaia* RP contaminants, it prejudices our results against classifying the most extreme spectral outliers, as was expected for extreme and ultra-subdwarfs. Thus, our expected number of 'prime candidates' was diminished.

The RP spectra of these 21 205 objects were extracted with GAIAXPY.CONVERT (Ruz-Mieres 2022) through the GAIAXPY-BATCH package (Cooper 2022). The absolute sampling of the retrieved spectra is a linearly dispersed grid from 600 to 1050 nm. We used this wavelength sampling (and only plot RP spectra within that limit) because it roughly corresponds to the *Gaia* DR3 RP passband (≈620–1042 nm; Riello et al. 2021). All spectra were divided by the sum of the fluxes across the entire 600–1050 nm region (i.e. the total flux of normalized spectra is unity). This method of normalization was chosen because other methods (e.g. dividing by a median flux of a given wavelength regime) could cause non-physical artifacts, especially for noisy spectra. Some *Gaia* RP spectra can exhibit *apparent* negative fluxes, as a result of the projection onto the Hermite base functions during their construction. We sample the wavelengths with a consistent linearly dispersed grid. Ergo, when one normalizes all of the *Gaia* RP spectra by dividing by the sum of the fluxes, the spectra are homogeneous in wavelength and absolute flux calibration, thus are comparable.

Instead of using an absolute magnitude to find outliers, such as the robust M_G to spectral type relation, the *Gaia* DR3 RP spectral sequence follows the optical spectral features which define spectral sub-types for different UCDs. Additionally, as discussed by Gaia Collaboration et al. (2021), there is a large scatter in *Gaia* colours for UCDs for every spectral type bin. This scatter, present in all photometric selections, means the introduction of a large number of contaminants. Using spectra instead might prove a cleaner selection technique, even at the low resolution of *Gaia* DR3 RP spectra.

In this section, we discuss the additional data gathering used to complement *Gaia* DR3. This includes the cross-matching with external photometry as well our basic spectral typing method. The external photometry was used for validation in Section 3,whilst the spectral typing was used to define bins when searching for outliers. We defined a new colour ratio and used this colour ratio to separate outlying UCDs from normal UCDs.

2.1 External cross-matching

Using the *Gaia* data archive, we first performed a `'left join'` query against the pre-computed cross-matches for Pan-STARRS (Chambers et al. 2016), 2MASS (Skrutskie et al. 2006) and AllWISE (Cutri et al. 2013). From these cross-matches we noted that the Pan-STARRS join was much less complete than 2MASS or AllWISE. As such, Pan-STARRS was not used in the photometric analysis but was used for the further discussion on our prime candidates. The RP spectral sample was cross-matched with the GUCDS. The GUCDS contains thousands of known objects with spectral types from the literature. Of these, ≈270 are known subdwarfs, and are flagged as such within their spectral types. This cross-matched sample between our 21 205 sample, and the GUCDS, is of size 2565. The known subdwarfs and young objects from this GUCDS cross-match are shown in Appendix Table A1 and were converted into Boolean flags from which we trained our candidate flagging techniques discussed below. Additionally, there exists a list of optical standards for a range of spectral types (see table 1, Sarro et al. 2023), which we use as part of our method and analysis. This list of standards was supplemented with tens of visually selected bright RP spectra which were as similar as possible to each standard; the final list is hereafter referred to as 'known standards' and shown in orange in Fig. 2.

2.2 Estimating a spectral type

For discussing our objects on an individual basis, it is more meaningful to write in terms of spectral type than $T_{\rm eff}$. As such, we discuss here a simplistic method for estimating spectral type from the $T_{\rm eff}$ values provided by *Gaia* DR3, `teff_espucd`. These spectral types estimated here were not used for any analysis. To more correctly ascertain spectral types, one would match the features and shapes of the RP spectra to well-known standards. This, however, is similar to our outlier detection technique, hence we seek to avoid any 'cyclic' analysis. All sources in our RP spectral sample have a derived effective temperature from *Gaia* DR3. However, known objects, including subdwarfs and young objects, are defined by their spectral types ('SpT', as that is a direct measurement) rather than effective temperatures, which are generally inferred from modelling. In the case of *Gaia* DR3, this modelling was trained on an empirical sample not containing any abnormal objects, like subdwarfs and young objects (Creevey et al. 2023; Sarro et al. 2023). Spectral type is known to have a direct relation to effective temperature, although there is significant scatter in $T_{\rm eff}$ for every spectral type. To convert the *Gaia* `teff_espucd` into a spectral type, we derived a fourth-order polynomial between the *Gaia* `teff_espucd` values and the GUCDS optical spectral types. This is shown in Fig. 3. This polynomial follows equation (1) with coefficients from Table 1, where spectral types are converted to numerical values using a code whereby M0 = 60, L0 = 70, T0 = 80, etc.:

$$\mathrm{SpT} = a{\mathrm{T}_{\rm eff}}^4 - b{\mathrm{T}_{\rm eff}}^3 + c{\mathrm{T}_{\rm eff}}^2 - d\mathrm{T}_{\rm eff} + e. \quad (1)$$

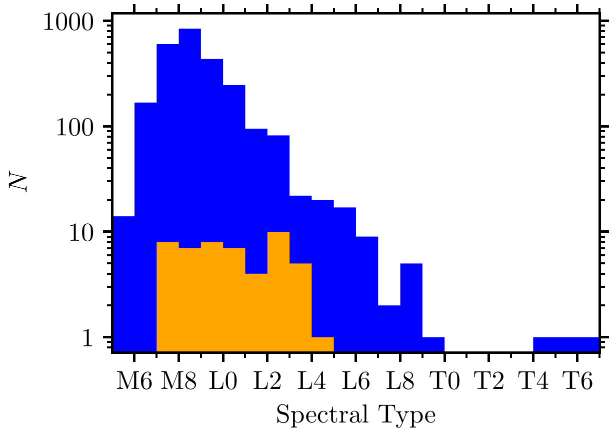

Figure 2. Histogram of the number of objects in each spectral type bin from the GUCDS. The full GUCDS is shown in blue whilst over plotted in orange is the distribution of the known standards used.

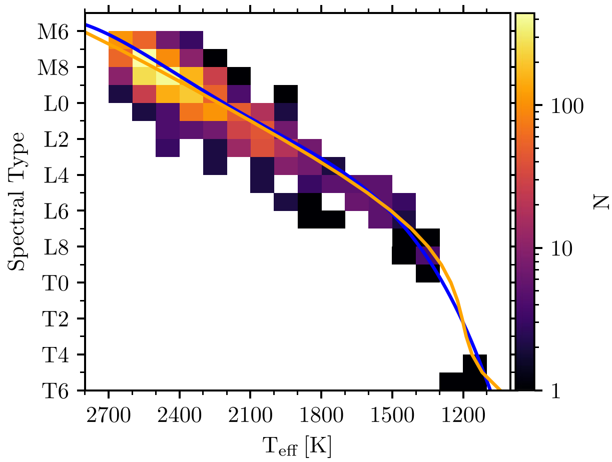

Figure 3. Spectral type conversion from $T_{\rm eff}$ (K) to spectral type for the GUCDS, as a 2D histogram. The number of objects in each bin is shown by the colour bar. Our fourth order polynomial is shown as the blue line. By comparison, we plot in orange the fifth-order polynomial (equation 4, Stephens et al. 2009) relation, valid from M6 to T8. A wider spread of $T_{\rm eff}$ can be seen in the late M and early L dwarfs. This is a natural spread as each known spectral type will have an error margin of one to two spectral types.

Table 1. Polynomial coefficients for $T_{\rm eff}$ to spectral-type relation in equation (1).

a	6.38 ± 1.07	10^{-12}	K^{-4}
b	5.61 ± 0.88	10^{-8}	K^{-3}
c	1.83 ± 0.27	10^{-4}	K^{-2}
d	2.71 ± 0.35	10^{-1}	K^{-1}
e	227 ± 17		K

Note. Valid for $1150 < T_{\rm eff} < 2700$ K or M6–T4.

2.3 Creating a colour ratio

Following literature definitions of spectral indices in the optical regime[1] (Kirkpatrick et al. 1999; Martín et al. 1999; Geballe et al. 2002), we created a method for measuring a colour ratio (CR). This method used directly the `teff_espucd` values in bins of 100 K. We note here that one spectral type is not equivalent to 100 K, i.e. $\Delta 100\,{\rm K} \neq \Delta$ 1SpT. As for the change in terminology from 'spectral index' to 'colour ratio', this is because the internally calibrated *Gaia* RP spectra as shown in Fig. 1 are too low resolution to use standard spectral typing indices. This method created photometric bands centred on the two primary peaks one can see in the internally calibrated *Gaia* RP spectra (Fig. 1). Gaia Collaboration et al. (2023b) discuss the creation of synthetic photometry from *Gaia* XP spectra, which inspired our method. Due to the redshifting of these peaks with decreasing effective temperature we define two spectral $T_{\rm eff}$-specific narrow bands (with width 50 nm), named '`blue`' and '`red`', respectively, where the central wavelength shifts with spectral type. These central wavelengths are the vertical dashed lines shown in Fig. 1. We linearly interpolate between each manually defined central wavelength against $T_{\rm eff}$ to account for the non-rounded $T_{\rm eff}$ values. The total region possibly bound by this relation is 795–995 nm, i.e. the lowest and highest wavelength within 25 nm of the central wavelengths.

These regions were decided by visually inspecting the known standards, subdwarfs, and young objects from the literature (Fig. 4). The flux summed in `blue`, divided by the flux summed in can be deemed a '`colour`'. To create CR we had to compare an object's observed `colour` to an 'expected' `colour`.

We constructed a median RP normalized spectrum for every 100 K bin (using the *Gaia* $T_{\rm eff}$, `teff_espucd`). Then we determined the `colour` for each median (i.e. the 'expected' `colour`). We created a linear spline relation between $T_{\rm eff}$ and this expected `colour`. Then, for every object, we measure the observed `colour` and compare it with the expected `colour`, extracted from the linear spline for that object's $T_{\rm eff}$. CR is each object's observed `colour` divided by the expected `colour`, rounded to two decimal places.

We sought outliers from CR to define candidate objects. Values of CR near 1 mean that object is normal. The median RP spectra of known objects are shown in Fig. 1, having been selected from the GUCDS by each spectral type bin from M5 to T6. We used median RP spectra instead of the known standards in our CR derivation method because of the larger amount of objects and wider spectral coverage, with the numbers of objects per spectral type bin shown in Fig. 2. In our `colour` region, the median RP spectra per spectral type differ from the known standards by $|\Delta F| \leq 10$ per cent. The major caveat for this method is that the `teff_espucd` values were generated from a training set which contained no outliers. Hence, it can be expected to be biased. We may be comparing an observed `colour` against expectations from an incorrect bin.

[1]Most spectral indices for UCDs are defined in the near-infrared rather than the optical; see Reid et al. (2001), Burgasser et al. (2006), Bardalez Gagliuffi et al. (2014), and references therein.

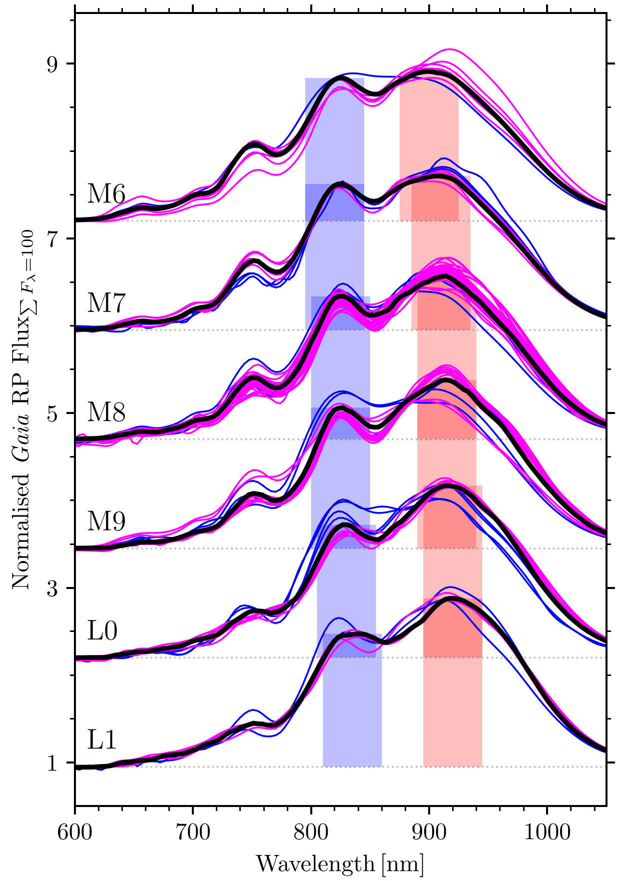

Figure 4. Internally calibrated RP spectra of known objects, separated by their literature optical spectral types. Magenta spectra are known young objects whilst blue spectra are known subdwarfs. Over-plotted in black is the median RP spectra for a given spectral type from known objects in the GUCDS. The `blue` and bands are shown in their respective positions and colours as described in Section 2.3. The normalized spectra were multiplied by a constant value such that the fluxes sum to 100 instead of 1 and are offset by a set value.

2.3.1 Determining outliers

For each object, the outliers were defined as the cases where CR was more than 3σ from the average value μ of all elements of CR ($\mu = 0.98 \pm 0.05$). Assuming a Gaussian distribution (z) centred at μ, this $\pm 3\sigma$ equated to the 0.01 per cent and 99.9 per cent percentiles (p) of z_p. In terms of CR, the 0.01 per cent percentile, $z_{-3\sigma}$, equals 0.80 whilst the 99.9 per cent percentile, $z_{3\sigma}$, equals 1.16. To summarize, this outlier selection was $z_{-3\sigma} \geq {\rm CR} \geq z_{3\sigma}$ or $0.80 \geq {\rm CR} \geq 1.16$ where $p = \pm 3\sigma$. This process went through multiple iterations of different bin sizes, `blue` and definitions (e.g. shifting with spectral type and not), numerical methods of creating CR, and different CR cut-off points. We chose the final method parameters such that it only selects the most extreme outliers. Under this selection criteria, subdwarf candidates were the objects with ${\rm CR} \geq z_{3\sigma}$ whilst young candidates had ${\rm CR} \leq z_{-3\sigma}$.

3 ANALYSIS

We discuss here methods of selecting interesting sub-samples of the candidate objects found by the CR in Section 2.3.1, although we provide the CR measure for every object. This analysis section is intended to produce a list of 'prime' candidates, which are the objects passing strict selection criteria. The aforementioned known standard

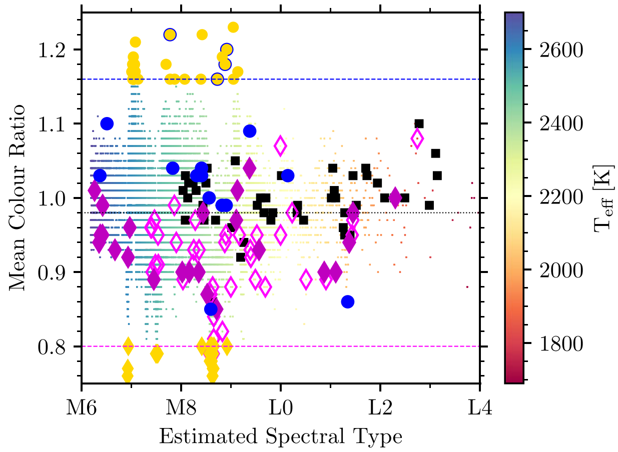

Figure 5. Colour ratio (CR, Section 2.3.1) against estimated spectral type (Section 2.2). We display sources only between M6–L4 (there are no later candidates). The full population is shown as small squares using a colour-code reflecting $T_{\rm eff}$ shown on the right-hand axis. Standards are displayed as black squares whilst known young objects are magenta diamonds (filled if very low gravity, i.e. δ/'vl-g') and known subdwarfs are blue circles. Horizontal coloured lines are shown demarcating the selection criteria, magenta for $\texttt{CR} \leq z_{-3\sigma}$ and blue for $\texttt{CR} \geq z_{3\sigma}$. A black dotted line is shown at the mean CR. Candidate subdwarfs are shown as yellow circles, while candidate young objects are shown as yellow diamonds.

sample was used to calibrate our CR values, and ensure we were not selecting 'normal' objects.

We defined any object with $\texttt{CR} \geq z_{3\sigma}$ as a CR-candidate subdwarf and anything with $\texttt{CR} \leq z_{-3\sigma}$ as a CR-candidate young object. This selection process is shown in Fig. 5.

There was an overdensity of sources around M7–M8, and therefore a less reliable median RP spectrum, hence the larger CR scatter and artifacts shown in Fig. 5. This is due to the artificial upper limit of $T_{\rm eff} < 2700$ K in `teff_espucd`.

Out of 21 205 RP spectra, 58 passed the aforementioned CR cuts. Following the discussion in section 3 by Sarro et al. (2023), we used internally calibrated RP spectra instead of externally calibrated RP spectra. This is because, as shown by spectral-type standards in Fig. 6, the external calibration produces non-physical artifacts for some UCDs (Carrasco et al. 2021; Montegriffo et al. 2023). It was not entirely predictable which objects saw the worst performance in the external calibration; however, generally the least bright and least observed (`phot_rp_n_obs`) objects had less reliable spectra. This is due to the external calibration being derived with sources outside of the UCD regime (Pancino et al. 2012). *Gaia* observes internally calibrated spectra, not externally calibrated ones. We base our analysis on a set of spectra that has not undergone an additional calibration stage which was not optimized for these red and faint sources. External calibration may introduce systematics upon which we have no control, in the context of a problem where the signal is very weak. The internally calibrated RP spectra showed a much cleaner spectral sequence, which was vital for determining if a given object is 'typical' in appearance for a given spectral type, or not. Both the internal and external calibration spectra were converted from physical wavelengths to 'pseudo-wavelengths' (used by `gaiaxpy`) via the dispersion function shown in fig. 9 from Montegriffo et al. (2023) and discussed in section 3.1 from De Angeli et al. (2023). This dispersion function is available through `gaiaxpy` and documented as `ExternalInstrumentModel.wl_to_pwl`. Flux uncertainties were larger in the external calibration, as shown in

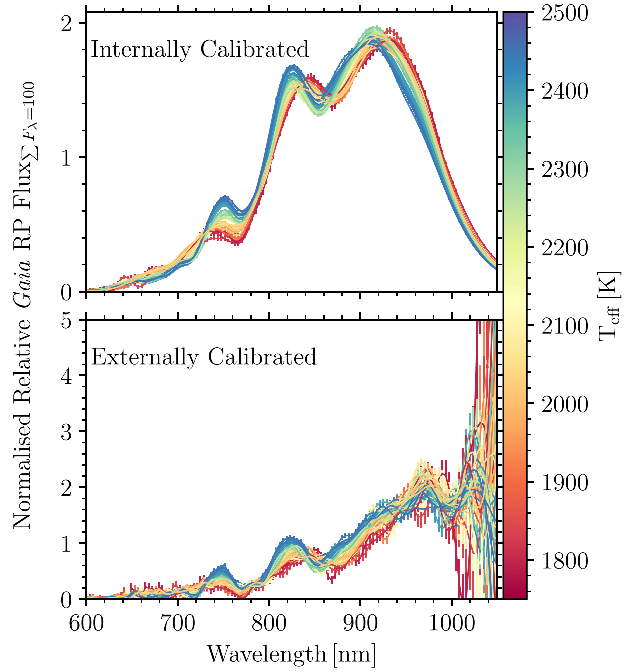

Figure 6. Spectral comparison between internally and externally calibrated RP spectra of spectral-type standards from M7 to L4. Spectra are coloured by effective temperature. Internally calibrated RP spectra of spectral type standards in the upper plot. Externally calibrated RP spectra of spectral type standards in the lower plot. The normalized spectra were multiplied by a constant value such that the fluxes sum to 100 instead of 1.

Fig. 6. One explanation for this is the known issue in *Gaia* DR3 that the internal calibration flux uncertainties are underestimated. The external calibration did have a larger relative range of fluxes from $F_{\rm min}$–$F_{\rm max}$ across our 795–995 nm region (Section 2.3). Such a larger relative range would produce improved discernment between neighbouring objects.

3.1 Photometry checks

In the optical regime of *Gaia*, subdwarfs are known to be typically blue objects whilst young objects are overluminous and red. As such, we constructed a CMD to check that candidate objects are in the same colour-space as known subdwarfs or known young objects. This is shown in Fig. 7. To do this, we created a selection of photometric cuts in Table 2. These are conservative selections on the two categories, aimed at selecting the bluest known subdwarfs and brightest known young objects. We made the selections conservative in order to avoid contaminant sources, as most contaminants are within the inherent CMD scatter on the UCD main sequence.

There are 906 candidate young objects and 260 candidate subdwarfs purely from the photometric cuts in Table 2. However, only one object is both a CR candidate, and a photometric young candidate, whilst six objects are both CR candidates, and photometric subdwarf candidates.

3.2 Kinematics

We provide a kinematic classification system to indicate thin disc, thick disc, and halo, based on each object's space motions. These motions were calculated using the equations from ASTROLIBPY, which follows the work by Johnson & Soderblom (1987), except

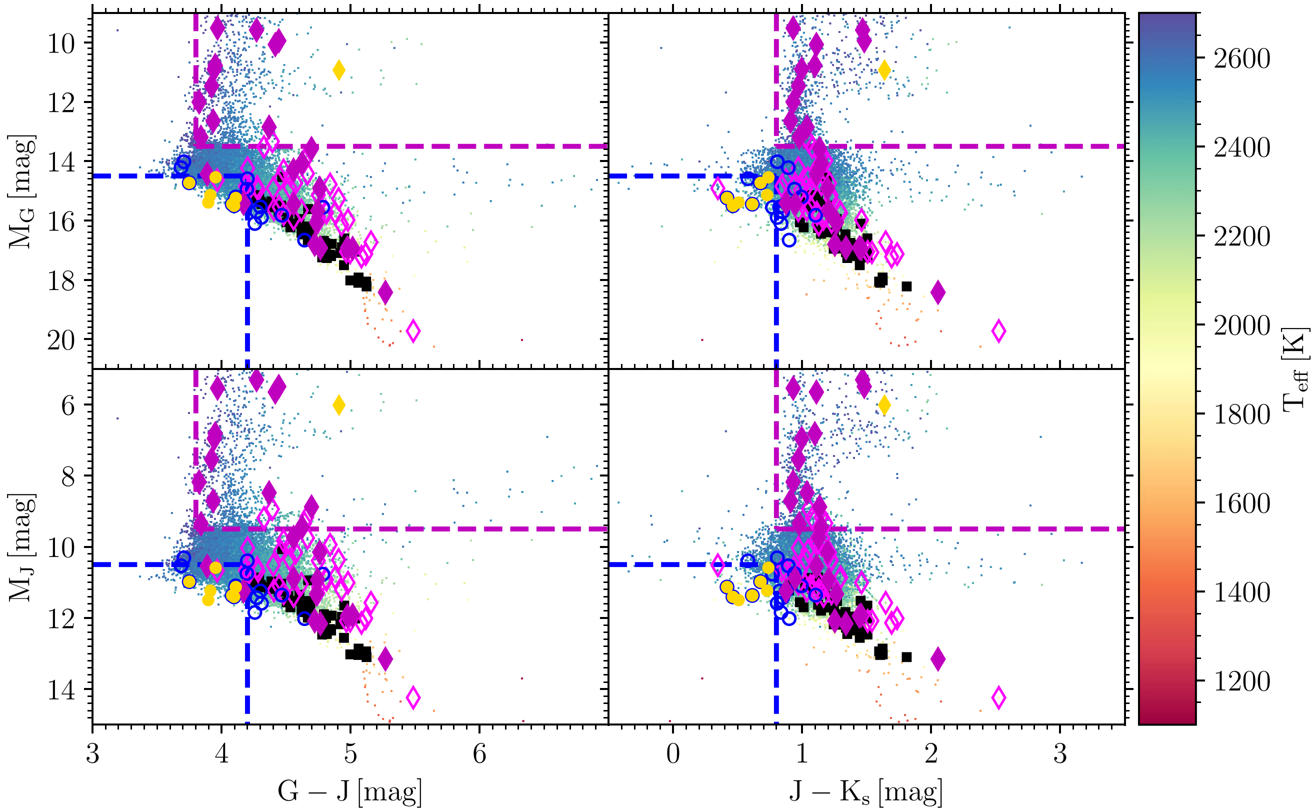

Figure 7. Four colour–absolute magnitude diagrams with M_G on the top row, M_J on the bottom row, $G-J$ on the left column, and $J-K_s$ on the right column. The full RP spectral sample is shown as small squares using a colour-code reflecting $T_{\rm eff}$, as shown in the colour bar. Standards are displayed as black squares whilst known young objects are open magenta diamonds (filled if very low gravity δ/'vl-g') and known subdwarfs are open blue circles. Candidate subdwarfs are own as yellow circles, whereas candidate young objects are shown as yellow diamonds. Dashed lines are shown demarcating the cut-offs for the photometric filtering of the candidate selection. Magenta lines show the young object candidate selection, and blue lines show the subdwarf selection. These lines represent the cuts in Table 2.

Table 2. Photometric cuts to select subdwarfs and young objects.

Subdwarf	Young
$M_G > 14.5$	$M_G < 13.5$
$G-J < 4.2$	$G-J > 3.8$
$M_J > 10.5$	$M_J < 9.5$
$J-K_s < 0.8^\star$	$J-K_s \geq 0.8$

Note. ⋆Slightly more liberal than the $J-K_s < 0.7$ cut by Lodieu et al. (2012).

that U is defined as positive towards the Galactic anti-centre. We used the Local Standard of Rest (LSR) from Coşkunoğlu et al. (2011) with U, V, W = (−8.50, 13.38, 6.49 km s^{-1}). To create UVW velocities, we needed radial velocities to complement the 5D astrometry from *Gaia* DR3.

We cross-matched our sample of 21 205 objects with *Gaia* RP spectra with SIMBAD (Wenger et al. 2000). This provided 2187 UCDs with literature radial velocities. For sources without radial velocities we estimated probability density distributions of the total velocity by assuming a normal radial velocity distribution. This distribution was obtained by a maximum likelihood fit to the values available from the literature, where $\mu = 0.2\,{\rm km\,s^{-1}}$, $\sigma = 52.3\,{\rm km\,s^{-1}}$. We sampled 1000 random radial velocities from this normal distribution for each object in our full sample. Therefore, each object had 1000 different UVW velocities. This converted into 1000 $V_{\rm total}$ values through $V_{\rm total} = \sqrt{U^2+V^2+W^2}$. From each object's range of $V_{\rm total}$ values, we extracted probabilities (P) of Galaxy component membership (thin disc, $P_{\rm thin}$; thick disc, $P_{\rm thick}$; halo, $P_{\rm halo}$). This assumes that U, V, W, and $V_{\rm total}$ are Gaussian distributions propagated from the normal radial velocity distribution and ignores the impact of metallicity on thick disc/halo discrimination. To do so, we calculated the survival function.[2] of each object's total velocity distribution at two critical velocities: 70 km s^{-1}and 180 km s^{-1} (Nissen & Schuster 2010). These are checked in descending order: $P_{\rm halo} = P(V_{\rm total} > 180\,{\rm km\,s^{-1}})$, $P_{\rm thick} = \max\{0,\ P(V_{\rm total} > 70\,{\rm km\,s^{-1}}) - P_{\rm halo}\}$, $P_{\rm thin} = \max\{0, 1. - P_{\rm thick} - P_{\rm halo}\}$. We then select the Galaxy component for each object as whichever probability is highest.

Of our candidates, subdwarf candidates were those objects in the halo (27) or thick disc (3701), whilst we required young objects to be in the thin disc (although some known young objects can be in the thick disc). Nevertheless, for young candidates, one object passed all of the respective CR, photometric and kinematic cuts. For the subdwarf candidates, six objects passed all of the respective CR, photometric, and kinematic cuts. These seven objects are our prime candidates. We present the surviving candidates on the Toomre diagram in Fig. 8, using the mean (of the 1000 total) UVW velocities with propagated uncertainties shown.

4 RESULTS

We present the *Gaia* RP spectra of the final, seven prime candidates, having survived all CR, photometric, and kinematic cuts in Fig. 9

[2]Equivalent to 1 − CDF (cumulative distribution function).

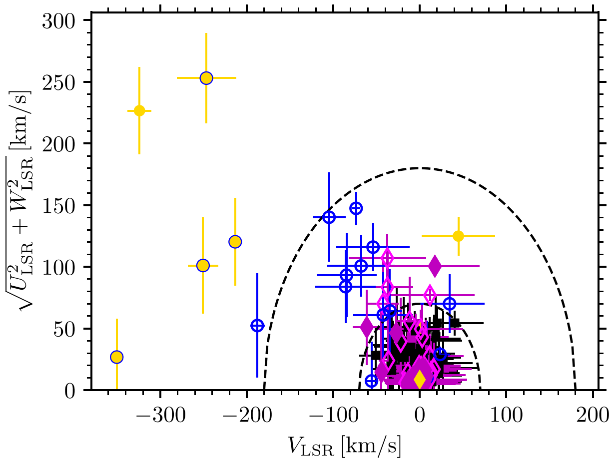

Figure 8. Toomre diagram (Sandage & Fouts 1987), corrected for the LSR, of our prime candidates with thick disc and halo selection lines shown at $V_{\rm total} > 70\,{\rm km\,s^{-1}}$ and $V_{\rm total} > 180\,{\rm km\,s^{-1}}$, respectively. Standards are displayed as black squares whilst known young objects are open magenta diamonds (filled if very low gravity δ/'vl-g') and known subdwarfs are open blue circles. Candidate subdwarfs are shown as yellow circles, whereas candidate young objects are shown as yellow diamonds. Error-bars in matching colours are also shown.

with their astrometry, spectral type, and $T_{\rm eff}$ shown in Table 3. We also show the stellar energy distribution (SED) difference from a normal SED of the same spectral type, for each object in Fig. 10.

We discuss here each object classified as a prime candidate in this work. Four candidates were already known subdwarfs and flagged as such in the GUCDS:

(i) **SSSPM J1444 − 2019** *(J1444 − 2019)*. In the literature, this object is an M9 (Bardalez Gagliuffi et al. 2014) or an sdL0 (in both the optical and near-infrared regime; Kirkpatrick et al. 2016). This work estimated a spectral type of M9, CR = 1.18 and $P_{\rm halo} = 1$. Our spectral type agrees with the literature's modal spectral type and our kinematics combined with its blue nature confirm the subdwarf.

(ii) **2MASS J14114474 − 4524153** *(J1411 − 4524)*. J1411 − 4524 is an sdM9 (Kirkpatrick et al. 2016). We found a spectral type of M8, CR = 1.22 and $P_{\rm halo} = 1$, hence our agreed classification as a subdwarf.

(iii) **2MASS J04353511 + 2115201** *(J0435 + 2115)*. An sdL0 (optical) object (Kirkpatrick et al. 2014), confirmed by Kirkpatrick et al. (2016) with a similar sdM9 from Luhman & Sheppard (2014).[3] The spectral type from this work is M8.5, mostly in agreement with the literature, with CR = 1.16 and $P_{\rm halo} = 1.0$. We concur with the subdwarf classification.

(iv) **2MASS J03060140 − 0330438** *(J0306 − 0330)*. Similarly, an sdL0 (optical) object (Kirkpatrick et al. 2014) with an sdM9 sub-type from Luhman & Sheppard (2014)[3]. This work estimated a spectral type of M9. CR = 1.20 and $P_{\rm halo} = 1.0$, the high CR value indicates this object is a likely subdwarf.

[3]There appears to be some confusion in the literature bibliography codes (bibcodes) about the origin of this spectral type. There are three very similar bibcodes: Luhman & Sheppard (2014ApJ...787..126L – 'Characterization of High Proper Motion Objects from the Wide-field Infrared Survey Explorer' 2014); Luhman (2014ApJ...786L..18L – 'Discovery of a ∼250 K Brown Dwarf at 2 pc from the Sun' 2014b); Luhman (2014ApJ...781....4L – 'A Search for a Distant Companion to the Sun with the Wide-field Infrared Survey Explorer' 2014a); the correct reference is Luhman & Sheppard (2014).

Two new subdwarf candidates were also found:

(i) **2MASS J03405673 + 2633447** *(J0340 + 2633)*. Not known to SIMBAD (besides an entry for *Gaia* DR3 and 2MASS) or the GUCDS.[4] We found a spectral type of M8.5, CR = 1.16 and $P_{\rm halo} = 1.0$. The CR value is on the borderline of the cut-off; however, this is still significant, especially considering that it has the fastest $V_{\rm tan}$ in the sample at $407.3\,{\rm km\,s^{-1}}$. It shows a non detection in PS1 g & r and is generally underluminous in the NIR (Fig. 10) but overluminous in the two reddest bands of AllWISE, a similar pattern to J0435 + 2115 (the known subdwarf of the same estimated spectral type). The missing detection in PS1 is due to the cross-matching, when visually inspected there is a highly red object visible within ≈2 arcsec. J0340 + 2633 is even more blue in Fig. 7 than most of our known subdwarfs, as would be expected for an extreme object.

(ii) **2MASS J01204397 + 6623543** *(J0120 + 6623)*. Likewise, this object has a lack of information in the literature. This work estimated a spectral type of M9, with CR = 1.19 and $P_{\rm thick} = 1.0$. The very high CR value also indicates this object is also non-standard for an M9. It also shows a non detection in PS1 g & r but additionally no match in AllWISE. This is again due to the cross-matching uncertainties as there is a clear red object in PS1 when visually inspected. It appears in the AllWISE images that the object is hidden by two neighbouring bright stars. However, it is *tending* towards being underluminous in the NIR (Fig. 10), as would be expected from the two known subdwarfs of the same estimated spectral type (J1444 − 2019 and J0306 − 0330). As with J0340 + 2633, J0120 + 6623 is notably more blue than other subdwarfs known to the literature in Fig. 7. This is therefore classed as a new subdwarf.

Additionally, we found one young object candidate, already known to the literature:

(i) **[BLH2002] KPNO−Tau 14** *(J0433 + 2616)*. This object is not in the GUCDS[4] but is an M7.2 (Zhang et al. 2018) in SIMBAD and classed as M6Ve by Luhman et al. (2003). Kounkel et al. (2019) give this object a radial velocity of 17.07 ± 0.37, which, combined with the $V_{\rm tan}$ of $13.84\,{\rm km\,s^{-1}}$, suggests it is strongly within the thin disc. It has also been repeatedly shown to be a member of the Taurus star-forming complex (Luhman et al. 2006; Kraus & Hillenbrand 2007; Luhman et al. 2010; Rebull et al. 2010; Luhman 2018; Rebull et al. 2020) and generally within the Taurus-Auriga ecosystem (Kraus et al. 2017). It is a young stellar object (YSO) with an age (from membership of Taurus) of 1–2 Myr (Gagné et al. 2018). Our spectral type is M8.5, within 2σ of the literature values, which is most likely due to the $T_{\rm eff}$ scatter in that spectral-type bin (see Fig. 3), in addition to the fact that YSOs are highly variable. The CR = 0.83 and $P_{\rm thin} = 0.8$. Fig. 10 shows this object is significantly overluminous for its spectral type, again typical of a YSO.

5 DISCUSSION

This work has produced a list of 58 objects, which have *Gaia* RP spectral differences greater than 3σ from median RP spectra, derived using the GUCDS and a new colour ratio (CR) specific to internally calibrated *Gaia* RP spectra. We finally produced a list of seven prime candidates, which have passed highly restrictive photometric and kinematic selections, aimed at recovering the most extreme objects in the sample.

[4]This is not unexpected, as the GUCDS is only intended to be complete for L dwarfs.

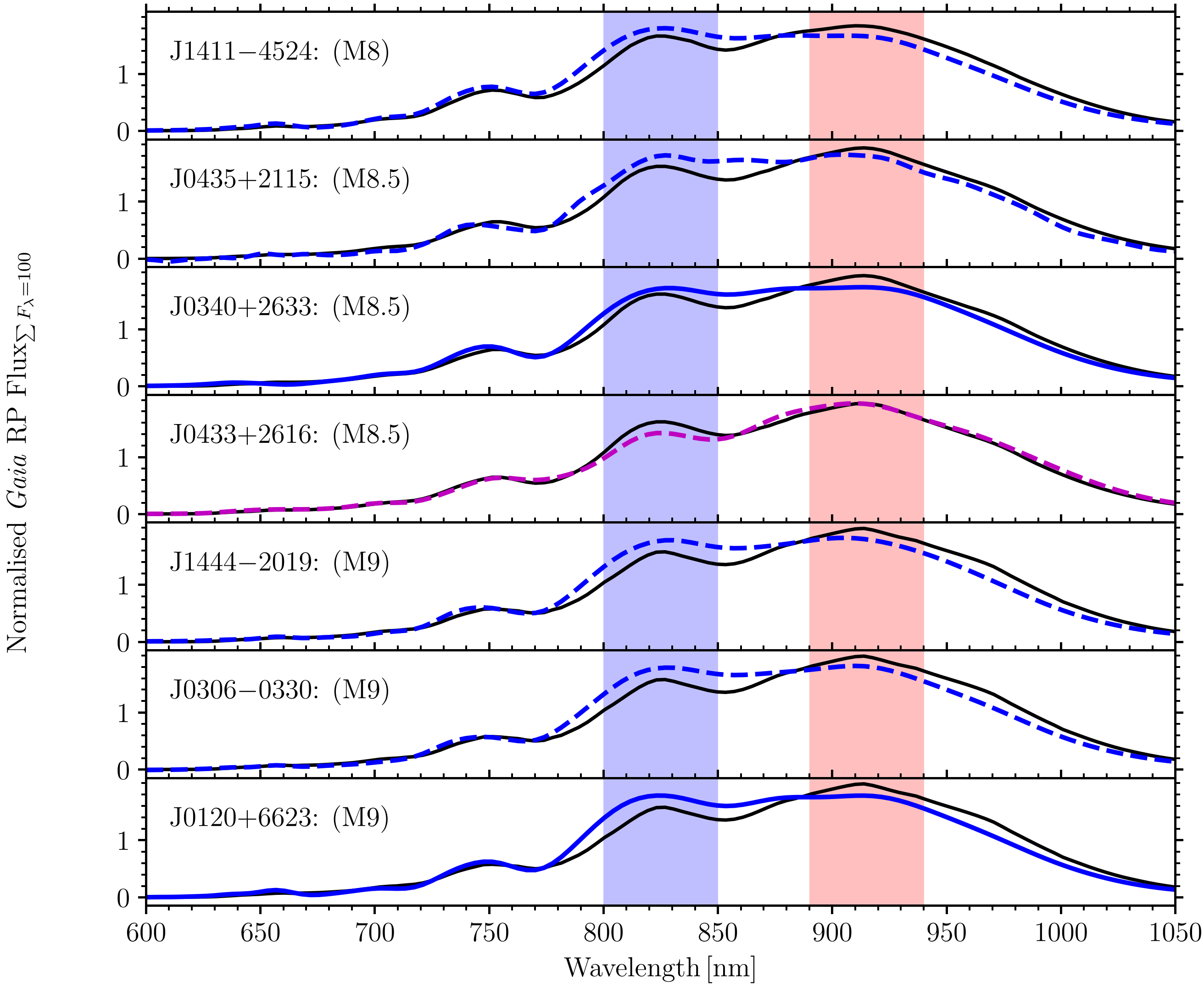

Figure 9. Internally calibrated RP spectra of our seven prime candidates with estimated spectral type, rounded to 0.5, indicated. Any objects with dashed lines are already known to the literature. Blue lines are subdwarfs whilst magenta lines are young objects. Over-plotted in black is the median RP spectra for the given spectral type from known objects in the GUCDS. Subdwarfs are typically overluminous in `blue` and underluminous in (the `blue` and bands shown as shaded regions, as described in Section 2.3) with the inverse true for young objects. The normalized spectra were multiplied by a constant value such that the fluxes sum to 100 instead of 1.

Table 3. Unsorted list of candidate subdwarfs and young objects.

Gaia DR3 Source ID	α (h m s)	δ (d m s)	ϖ (mas)	Object name	Spectral type	$T_{\rm eff}$ (K)
6281432246412503424	14 44 17	−20 19 56.9	58.1 ± 0.1	SSSPM J1444 − 2019[1]	sdM9[2]	2352 ± 10
6096164227899898880	14 11 42	−45 24 20.1	19.1 ± 0.2	2MASS J14114474 − 4524153[3]	sdM9[4]	2487 ± 47
144711230753602048	4 35 36	+ 21 15 03.6	16.7 ± 0.6	2MASS J04353511 + 2115201[3]	sdL0[5]	2371 ± 74
5183457632811832960	3 06 02	−3 31 06.1	24.7 ± 0.3	2MASS J03060140 − 0330438[3]	sdL0[5]	2348 ± 55
70974545020346240	3 40 58	+ 26 33 40.8	10.6 ± 0.7	2MASS J03405673 + 2633447[6]	sdM8.5[7]	2411 ± 111
525463551877051136	1 20 44	+ 66 23 59.0	12.1 ± 0.4	2MASS J01204397 + 6623543[6]	sdM9[7]	2359 ± 106
151130591952773632	4 33 08	+ 26 16 06.3	6.6 ± 0.2	[BLH2002] KPNO−Tau 14[8]	M7.2[9]	2385 ± 18

References. 1. Scholz, Lodieu & McCaughrean (2004), 2. Winters et al. (2015), 3. Luhman (2014a), 4. Kirkpatrick et al. (2016), 5. Kirkpatrick et al. (2014), 6. Skrutskie et al. (2006), 7. This Work, 8. Luhman et al. (2003), 9. Zhang et al. (2018). *Note*. Astrometry is from *Gaia* DR3 and the $T_{\rm eff}$ values are those produced by the ESP-UCD Apsis module and published as part of the Data Release.

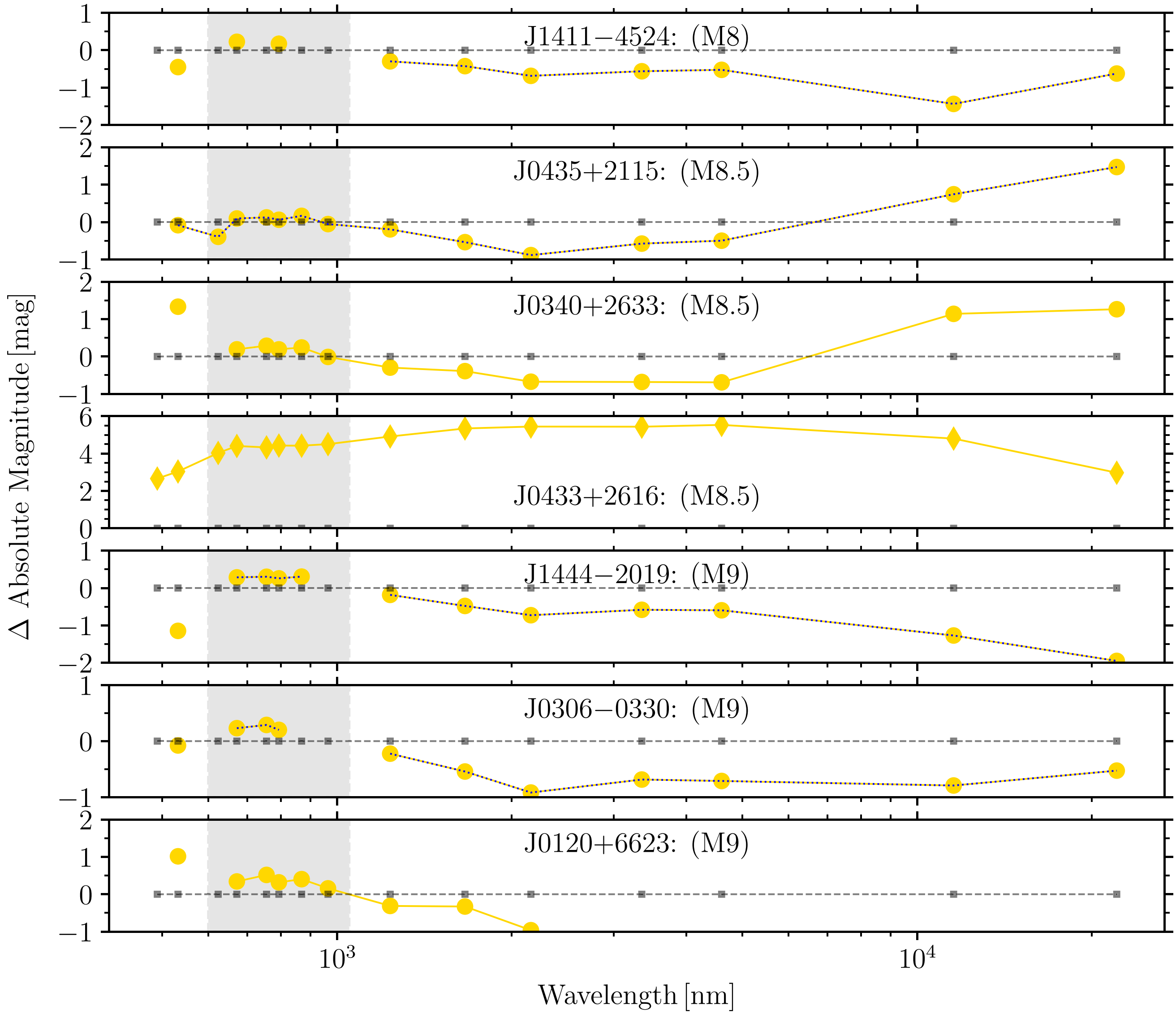

Figure 10. The Δ SEDs for our seven prime candidates in yellow with estimated spectral type (rounded to 0.5) indicated, as compared with the mean absolute magnitudes for the given spectral type from the GUCDS. Positive values indicate overbrightness and negative values underbrightness. Blue dotted lines are shown on the objects already known to be subdwarfs in the literature. Over-plotted in dark grey at zero are the wavelengths covered. A grey shading is shown in the region covered by *Gaia* RP spectra. The photometry shown is from Pan-STARRS, *Gaia*, 2MASS, and AllWISE; converted into an absolute magnitude using the *Gaia* DR3 parallax. The wavelengths plotted correspond to the mean wavelengths ($\bar{\lambda}$) of each photometric band (g, G_{BP}, r, G, i, G_{RP}, z, y, J, H, K_{s}, $W1$, $W2$, $W3$, $W4$, in increasing $\bar{\lambda}$ order), as extracted from VOSA (Bayo et al. 2008).

Whilst we could have used a more liberal set of cuts, the intention in this work was to produce the most confident candidates. Additionally, part of the publication criteria (see Section 2) for *Gaia* RP UCD spectra was that the RP spectra had the highest quality flags (`flags_espucd` 0–1). This meant objects with higher Euclidean distances from BT-Settl (Allard, Homeier & Freytag 2011) models (simulated through the *Gaia* RP transmission function) are not included. In other words, the most extreme objects we seek to classify were precluded from inclusion in *Gaia* DR3[5].

[5]However, the quality flag selections performed by ESP-UCD were very sensible (see the discussion by Creevey et al. 2023 and Sarro et al. 2023), as there were many potential contaminants and highly noisy spectra in the lowest quality flag (2).

Several other biases exist, such as the artificial cut of $T_{\mathrm{eff}} < 2700$ K from `teff_espucd`. This caused the over density seen at the M7–M8. The lack of outliers in the empirical training set in *Gaia* DR3 also caused a bias in the creation of expected `colour`. Also, the sample of known young objects and known subdwarfs in the GUCDS includes many objects, which appear not considerably different from a normal object when visually observed at a resolution as low as *Gaia* RP, see Fig. 4. This can be evidenced by Fig. 5, where there is little scatter in `CR` in spectral sub-types beyond L0. These objects are as equally interesting as extreme outliers, but require higher resolution optical and NIR spectroscopy to observe directly the features relating to surface gravity and metallicity. Many of these objects did not pass the `CR` selection, photometric and kinematic cuts, or both. These reasons combined with the rarity of extreme UCDs are the cause of there being so few prime candidates in our final list. However, the detection of the known extreme UCDs shown here is a highly promising baseline for future analysis. The additional detection of two unknown subdwarf candidates is demonstrative of the fact that existing datasets, like *Gaia* DR3, contain many interesting objects, still to be discovered. This future work could include more advanced selection techniques such as machine learning, more liberal selection criteria and the increased breadth and depth of planned *Gaia* data releases.

ACKNOWLEDGEMENTS

RLS and WJC were been supported by a STSM grant from COST Action CA18104: MW-Gaia. The authors would like to thank José Caballero at ESAC for his much appreciated advice. WJC was funded by a University of Hertfordshire studentship, and both WJC and HRAJ were supported by STFC grant ST/R000905/1 at the University of Hertfordshire. We would like to thank the anonymous reviewer for their timely and useful advice, which has much improved this technique and paper.

This publication makes use of reduction and data products from the Centre de Données astronomiques de Strasbourg (SIMBAD, cdsweb.u-strasbg.fr); the ESA *Gaia* mission (http://sci.esa.int/gaia) funded by national institutions participating in the Gaia Multilateral Agreement and in particular the support of ASI under contract I/058/10/0 (Gaia Mission – The Italian Participation to DPAC); the Panoramic Survey Telescope and Rapid Response System (Pan-STARRS, panstarrs.stsci.edu); the Sloan Digital Sky Survey (SDSS, www.sdss.org); the Two Micron All Sky Survey (2MASS, www.ipac.caltech.edu/2mass); and the *Wide-field Infrared Survey Explorer* (*WISE*, wise.ssl.berkeley.edu).

We acknowledge the relevant open source packages used in our PYTHON (van Rossum & de Boer 1991) codes: ASTROPY (Astropy Collaboration et al. 2013, 2018), MATPLOTLIB (Hunter 2007), NUMPY (Harris et al. 2020), PANDAS (McKinney 2010; The Pandas Development Team 2020), SCIPY (Virtanen et al. 2020), SYMPY (Meurer et al. 2017), TQDM (da Costa-Luis et al. 2021).

DATA AVAILABILITY

The data underlying this paper will be shared on reasonable request to the corresponding author. It will additionally be available through CDS VizieR.

REFERENCES

Aganze C. et al., 2016, AJ, 151, 46
Allard F., Homeier D., Freytag B., 2011, in Johns-Krull C., Browning M. K., West A. A., eds, ASP Conf. Ser. Vol. 448, 16th Cambridge Workshop on Cool Stars, Stellar Systems, and the Sun. Astron. Soc. Pac., San Francisco, p. 91
Allers K. N., Liu M. C., 2013, ApJ, 772, 79
Anders F., Khalatyan A., Queiroz A. B. A., Nepal S., Chiappini C., 2023, preprint (arXiv:2302.06995)
Andrae R., Rix H.-W., Chandra V., 2023, ApJS, 267, 8
Andrei A. H. et al., 2011, AJ, 141, 54
Ardila D., Martín E., Basri G., 2000, AJ, 120, 479
Astropy Collaboration et al., 2013, A&A, 558, A33
Astropy Collaboration et al., 2018, AJ, 156, 123
Bardalez Gagliuffi D. C. et al., 2014, ApJ, 794, 143
Bayo A., Rodrigo C., Barrado Y Navascués D., Solano E., Gutiérrez R., Morales-Calderón M., Allard F., 2008, A&A, 492, 277
Bouy H., Brandner W., Martín E. L., Delfosse X., Allard F., Basri G., 2003, AJ, 126, 1526
Burgasser A. J. et al., 2002, ApJ, 564, 421
Burgasser A. J., 2004, ApJ, 614, L73
Burgasser A. J., Geballe T. R., Leggett S. K., Kirkpatrick J. D., Golimowski D. A., 2006, ApJ, 637, 1067
Burgasser A. J., McElwain M. W., Kirkpatrick J. D., Cruz K. L., Tinney C. G., Reid I. N., 2004, AJ, 127, 2856
Carrasco J. M. et al., 2021, A&A, 652, A86
Chambers K. C. et al., 2016, preprint (arXiv:1612.05560)
Cieza L., Baliber N., 2006, ApJ, 649, 862
Cooper W. J., 2022, gaiaxpy-batch (1.2.0). Zenodo. Available at: https://doi.org/10.5281/zenodo.6653446
Coşkunoğlu B. et al., 2011, MNRAS, 412, 1237
Creevey O. L. et al., 2023, A&A, 674, A26
Cruz K. L. et al., 2007, AJ, 133, 439
Cruz K. L., Galindo C., Faherty J. K., Riedel A. R., BDNYC, 2016, American Astronomical Society Meeting Abstracts #227. p. 145.03
Cruz K. L., Kirkpatrick J. D., Burgasser A. J., 2009, AJ, 137, 3345
Cruz K. L., Reid I. N., Liebert J., Kirkpatrick J. D., Lowrance P. J., 2003, AJ, 126, 2421
Culpan R., Geier S., Reindl N., Pelisoli I., Gentile Fusillo N., Vorontseva A., 2022, A&A, 662, A40
Cushing M. C. et al., 2011, ApJ, 743, 50
Cutri R. M. et al., 2013, VizieR Online Data Catalog, p. II/328
da Costa-Luis C. et al., 2021, tqdm: A fast, Extensible Progress Bar for Python and CLI (v4.48.0). Zenodo. Available at: https://doi.org/10.5281/zenodo.3948887
De Angeli F. et al., 2023, A&A, 674, A2
Deacon N. R., Hambly N. C., 2007, A&A, 468, 163
Dupuy T. J., Liu M. C., 2012, ApJS, 201, 19
EROS Collaboration et al., 1999, A&A, 351, L5
Esplin T. L., Luhman K. L., Mamajek E. E., 2014, ApJ, 784, 126
Faherty J. K. et al., 2012, ApJ, 752, 56
Gagné J. et al., 2015a, ApJS, 219, 33
Gagné J., Lafrenière D., Doyon R., Malo L., Artigau É., 2015b, ApJ, 798, 73
Gagné J. et al., 2017, ApJS, 228, 18
Gagné J. et al., 2018, ApJ, 856, 23
Gagné J., Faherty J. K., 2018, ApJ, 862, 138
Gagné J., Faherty J. K., Cruz K., Lafrenière D., Doyon R., Malo L., Artigau É., 2014, ApJ, 785, L14
Gaia Collaboration et al., 2016, A&A, 595, A1
Gaia Collaboration et al., 2021, A&A, 649, A6
Gaia Collaboration et al., 2023a, A&A, 674, A1
Gaia Collaboration et al., 2023b, A&A, 674, A33
Gaia Collaboration et al., 2023c, A&A, 674, A39
Gálvez-Ortiz M. C. et al., 2014, MNRAS, 439, 3890
Geballe T. R. et al., 2002, ApJ, 564, 466
Gizis J. E., 1997, AJ, 113, 806
Gizis J. E., 2002, ApJ, 575, 484
Gizis J. E., Monet D. G., Reid I. N., Kirkpatrick J. D., Liebert J., Williams R. J., 2000, AJ, 120, 1085
Gizis J. E., Reid I. N., 1999, AJ, 117, 508
Gliese W., Jahreiß H., 1991, in Brotzmann L. E., Gesser S. E., eds, Preliminary Version of the Third Catalogue of Nearby Stars, On: The Astronomical Data Center CD-ROM: Selected Astronomical Catalogs, Vol. I. NASA/Astronomical Data Center, Goddard Space Flight Center, Greenbelt, MD
Harris C. R. et al., 2020, Nature, 585, 357
Hawley S. L. et al., 2002, AJ, 123, 3409
Hellemans A., 1998, Science, 282, 1240
Hunter J. D., 2007, Comput. Sci. Eng., 9, 90
Johnson D. R. H., Soderblom D. R., 1987, AJ, 93, 864
Katz D. et al., 2023, A&A, 674, A5
Kellogg K., Metchev S., Miles-Páez P. A., Tannock M. E., 2017, AJ, 154, 112
Kirkpatrick J. D. et al., 1999, ApJ, 519, 802
Kirkpatrick J. D. et al., 2008, ApJ, 689, 1295
Kirkpatrick J. D. et al., 2010, ApJS, 190, 100

Kirkpatrick J. D. et al., 2014, ApJ, 783, 122
Kirkpatrick J. D. et al., 2016, ApJS, 224, 36
Kirkpatrick J. D. et al., 2021, ApJS, 253, 7
Kirkpatrick J. D., 2005, ARA&A, 43, 195
Kirkpatrick J. D., Barman T. S., Burgasser A. J., McGovern M. R., McLean I. S., Tinney C. G., Lowrance P. J., 2006, ApJ, 639, 1120
Koppelman H., Helmi A., Veljanoski J., 2018, ApJ, 860, L11
Kounkel M. et al., 2019, AJ, 157, 196
Kraus A. L., Herczeg G. J., Rizzuto A. C., Mann A. W., Slesnick C. L., Carpenter J. M., Hillenbrand L. A., Mamajek E. E., 2017, ApJ, 838, 150
Kraus A. L., Hillenbrand L. A., 2007, ApJ, 662, 413
Leggett S. K., 1992, ApJS, 82, 351
Leggett S. K., Hawkins M. R. S., 1989, MNRAS, 238, 145
Lépine S., 2008, AJ, 135, 2177
Lépine S., Shara M. M., Rich R. M., 2002a, AJ, 124, 1190
Lépine S., Rich R. M., Neill J. D., Caulet A., Shara M. M., 2002b, ApJ, 581, L47
Lépine S., Rich R. M., Shara M. M., 2003, ApJ, 591, L49
Liebert J., Dahn C. C., Gresham M., Strittmatter P. A., 1979, ApJ, 233, 226
Lodieu N., Espinoza Contreras M., Zapatero Osorio M. R., Solano E., Aberasturi M., Martín E. L., 2012, A&A, 542, A105
Lodieu N., Espinoza Contreras M., Zapatero Osorio M. R., Solano E., Aberasturi M., Martín E. L., Rodrigo C., 2017, A&A, 598, A92
Looper D. L., Burgasser A. J., Kirkpatrick J. D., Swift B. J., 2007, ApJ, 669, L97
Luhman K. L., 2014a, ApJ, 781, 4
Luhman K. L., 2014b, ApJ, 786, L18
Luhman K. L., 2018, AJ, 156, 271
Luhman K. L., Allen P. R., Espaillat C., Hartmann L., Calvet N., 2010, ApJS, 186, 111
Luhman K. L., Briceño C., Stauffer J. R., Hartmann L., Barrado y Navascués D., Caldwell N., 2003, ApJ, 590, 348
Luhman K. L., Esplin T. L., Loutrel N. P., 2016, ApJ, 827, 52
Luhman K. L., Herrmann K. A., Mamajek E. E., Esplin T. L., Pecaut M. J., 2018, AJ, 156, 76
Luhman K. L., Mamajek E. E., Allen P. R., Cruz K. L., 2009, ApJ, 703, 399
Luhman K. L., Mamajek E. E., Shukla S. J., Loutrel N. P., 2017, AJ, 153, 46
Luhman K. L., Sheppard S. S., 2014, ApJ, 787, 126
Luhman K. L., Whitney B. A., Meade M. R., Babler B. L., Indebetouw R., Bracker S., Churchwell E. B., 2006, ApJ, 647, 1180
Magazzù A., Dougados C., Licandro J., Martín E. L., Magnier E. A., Ménard F., 2003, in Martín E., ed., Proc. IAU Symp. 211, Brown Dwarfs. Kluwer, Dordrecht, p. 75
Marocco F. et al., 2013, AJ, 146, 161
Marocco F. et al., 2017, MNRAS, 470, 4885
Marocco F. et al., 2020, MNRAS, 494, 4891
Martín E. L., Delfosse X., Basri G., Goldman B., Forveille T., Zapatero Osorio M. R., 1999, AJ, 118, 2466
McKinney W., 2010, in van der Walt S., Millman J., eds, Proceedings of the 9th Python in Science Conference. p. 56
Ménard F., Delfosse X., Monin J. L., 2002, A&A, 396, L35
Meurer A. et al., 2017, PeerJ Comput. Sci., 3, e103
Montegriffo P. et al., 2023, A&A, 674, A3
Nissen P. E., Schuster W. J., 2010, A&A, 511, L10
Pancino E. et al., 2012, MNRAS, 426, 1767
Phan-Bao N. et al., 2003, A&A, 401, 959
Rebull L. M. et al., 2010, ApJS, 186, 259
Rebull L. M., Stauffer J. R., Cody A. M., Hillenbrand L. A., Bouvier J., Roggero N., David T. J., 2020, AJ, 159, 273
Reid I. N., Burgasser A. J., Cruz K. L., Kirkpatrick J. D., Gizis J. E., 2001, AJ, 121, 1710
Reid I. N., Cruz K. L., Kirkpatrick J. D., Allen P. R., Mungall F., Liebert J., Lowrance P., Sweet A., 2008, AJ, 136, 1290
Reid I. N., Lewitus E., Allen P. R., Cruz K. L., Burgasser A. J., 2006, AJ, 132, 891
Reiners A., Basri G., 2006, AJ, 131, 1806
Reylé C., Jardine K., Fouqué P., Caballero J. A., Smart R. L., Sozzetti A., 2021, A&A, 650, A201
Riello M. et al., 2021, A&A, 649, A3
Ruz-Mieres D., 2022, gaia-dpci/GaiaXPy: GaiaXPy 1.1.4, Zenodo. Available at: https://doi.org/10.5281/zenodo.6674521
Salim S., Lépine S., Rich R. M., Shara M. M., 2003, ApJ, 586, L149
Sandage A., Fouts G., 1987, AJ, 93, 74
Sarro L. M. et al., 2023, A&A, 669, A139
Sartoretti P. et al., 2023, A&A, 674, A6
Schmidt S. J., Cruz K. L., Bongiorno B. J., Liebert J., Reid I. N., 2007, AJ, 133, 2258
Schneider A. C., Greco J., Cushing M. C., Kirkpatrick J. D., Mainzer A., Gelino C. R., Fajardo-Acosta S. B., Bauer J., 2016, ApJ, 817, 112
Schneider A., Melis C., Song I., Zuckerman B., 2011, ApJ, 743, 109
Scholz R. D., Lodieu N., McCaughrean M. J., 2004, A&A, 428, L25
Scholz R. D., McCaughrean M. J., Zinnecker H., Lodieu N., 2005, A&A, 430, L49
Schönrich R., Binney J., 2009, MNRAS, 399, 1145
Skrutskie M. F. et al., 2006, AJ, 131, 1163
Smart R. L., Marocco F., Caballero J. A., Jones H. R. A., Barrado D., Beamín J. C., Pinfield D. J., Sarro L. M., 2017, MNRAS, 469, 401
Smart R. L., Marocco F., Sarro L. M., Barrado D., Beamín J. C., Caballero J. A., Jones H. R. A., 2019, MNRAS, 485, 4423
Stephens D. C. et al., 2009, ApJ, 702, 154
The Pandas Development Team, 2020, pandas-dev/pandas: Pandas (v2.1.0). Zenodo. Available at: https://doi.org/10.5281/zenodo.8301632
Tinney C. G., 1993, ApJ, 414, 279
Tinney C. G., Reid I. N., 1998, MNRAS, 301, 1031
van Rossum G., de Boer J., 1991, CWI Q., 4, 283
Venn K. A., Irwin M., Shetrone M. D., Tout C. A., Hill V., Tolstoy E., 2004, AJ, 128, 1177
Virtanen P. et al., 2020, Nat. Methods, 17, 261
Wenger M. et al., 2000, A&AS, 143, 9
West A. A., Hawley S. L., Bochanski J. J., Covey K. R., Reid I. N., Dhital S., Hilton E. J., Masuda M., 2008, AJ, 135, 785
Wilson J. C., Miller N. A., Gizis J. E., Skrutskie M. F., Houck J. R., Kirkpatrick J. D., Burgasser A. J., Monet D. G., 2003, in Martín E.ed., Proc. IAU Symp. 211, Brown Dwarfs. Kluwer, Dordrecht, p. 197
Winters J. G. et al., 2015, AJ, 149, 5
Yao Y., Ji A. P., Koposov S. E., Limberg G., 2023, preprint (arXiv:2303.17676)
Zhang H. W., Zhao G., 2006, A&A, 449, 127
Zhang X., Green G. M., Rix H.-W., 2023, MNRAS
Zhang Z. et al., 2018, ApJ, 858, 41
Zhang Z. H. et al., 2017a, MNRAS, 464, 3040
Zhang Z. H., Homeier D., Pinfield D. J., Lodieu N., Jones H. R. A., Allard F., Pavlenko Y. V., 2017b, MNRAS, 468, 261
Zhang Z. H., Burgasser A. J., Smith L. C., 2019, MNRAS, 486, 1840

APPENDIX:

Table A1. List of sub-dwarfs and young onjects used to train our colour ratio.

Gaia DR3 Source ID	α ($^{\mathrm{h\,m\,s}}$)	δ ($^{\mathrm{d\,m\,s}}$)	ϖ (mas)	Object name	Spectral type	T_{eff} (K)
164802984685384320	4 15 41	+ 29 15 07.6	6.5 ± 0.1	2MASS J04154131 + 2915078[1]	M8γ[2]	2664 ± 13
4406489184157821952	16 10 28	−0 41 13.7	33.5 ± 0.3	LSR J1610 − 0040[3]	d/sdM6[4]	2651 ± 11
152466120624336896	4 26 45	+ 27 56 42.9	7.4 ± 0.1	2MASS J04264449 + 2756433[1]	M7γ[2]	2674 ± 19
3406128761895775872	4 44 02	+ 16 21 32.1	6.9 ± 0.1	2MASS J04440164 + 1621324[1]	M7γ[1]	2670 ± 14
52039511681854208	4 10 28	+ 20 51 50.5	7.7 ± 0.4	2MASS J04102834 + 2051507[1]	M7γ[1]	2688 ± 20
6412696995416769536	22 02 58	−56 05 10.0	14.4 ± 0.3	2MASS J22025794 − 5605087[5]	M6.2γ[6]	2322 ± 27
3311992669430199168	4 22 14	+ 15 30 52.6	3.5 ± 0.1	Cl∗ Melotte 25 LH 190[7]	M6:γ[8]	2527 ± 19
6154629964132559104	12 57 45	−36 35 43.4	12.3 ± 0.2	2MASS J12574463 − 3635431[5]	M6::γ[6]	2523 ± 40
6246004053326362368	16 17 43	−18 58 18.3	16.7 ± 0.5	2MASS J16174255 − 1858179[9]	s/sdM7[9]	2350 ± 224
152917298349085824	4 25 16	+ 28 29 27.1	7.2 ± 0.1	2MASS J04251550 + 2829275[10]	M7γ[2]	2628 ± 8
4364702279101281024	17 12 51	−5 07 36.8	43.5 ± 0.1	G 19 − 16B[11]	M7β[12]	2410 ± 55
6246979972975055360	15 57 52	−19 56 39.5	19.9 ± 0.4	UScoCTIO 135[13]	d/sdM7[9]	2391 ± 37
2497288672467622912	2 50 12	−1 51 30.4	19.7 ± 0.1	TVLM 831 − 154910[14]	M7.3γ[6]	2664 ± 20
638128236336998016	9 24 31	+ 21 43 51.9	9.9 ± 0.5	2MASS J09243114 + 2143536[15]	M7β[15]	2534 ± 61
5682841554856156160	9 17 11	−16 50 05.3	13.7 ± 0.3	SIPS J0917 − 1649[16]	M7β[15]	2532 ± 57
1191334936190541184	15 56 19	+ 13 00 53.4	10.9 ± 0.7	2MASS J15561873 + 1300527[17]	M8β[17]	2387 ± 153
1250625276082413568	13 54 43	+ 21 50 29.4	11.1 ± 0.3	2MASS J13544271 + 2150309[15]	M8γ[15]	2593 ± 49
1597899151767870208	15 41 24	+ 54 25 58.7	7.8 ± 0.4	2MASS J15412408 + 5425598[17]	sdM7.5[18]	2480 ± 140
1310888340170379136	16 39 08	+ 28 39 00.6	9.3 ± 0.5	2MASS J16390818 + 2839015[17]	M8β[15]	2516 ± 54
4562040220870331520	17 03 36	+ 21 19 03.1	12.8 ± 0.5	2MASS J17033593 + 2119071[15]	M8β[15]	2416 ± 135
6442586188225229312	20 11 57	−62 01 18.9	12.8 ± 0.4	2MASS J20115649 − 6201127[19]	sdM8[20]	2422 ± 51
4588438567346043776	18 26 08	+ 30 14 07.9	90.1 ± 0.1	LSR J1826 + 3014[21]	sdM8.5[18]	2360 ± 14
147786354323787008	4 34 06	+ 24 18 50.4	7.5 ± 0.2	2MASS J04340619 + 2418508[22]	M8γ[2]	2440 ± 67
1938820873903912448	23 36 38	+ 45 23 30.4	8.0 ± 0.7	2MASS J23363834 + 4523306[17]	M8β[17]	2531 ± 83
4693823801926111360	2 21 29	−68 31 40.1	14.4 ± 0.2	2MASS J02212859 − 6831400[23]	M8[23]	2471 ± 63
4708433867622492416	0 38 15	−64 03 53.7	21.8 ± 0.3	2MASS J00381489 − 6403529[5]	M8.2β[6]	2252 ± 63
5734132118729087488	8 56 14	−13 42 24.6	18.6 ± 0.2	2MASS J08561384 − 1342242[6]	M8.6β[6]	2380 ± 32
6258149537937551232	15 20 17	−17 55 34.5	21.5 ± 0.3	SIPS J1520 − 1755[16]	M8β[15]	2353 ± 63
4815936868977501568	4 36 28	−41 14 46.3	25.3 ± 0.1	2MASS J04362788 − 4114465[24]	M8$\beta\gamma$[25]	2429 ± 15
373562923829421440	1 14 58	+ 43 18 57.6	21.1 ± 0.4	2MASS J01145788 + 4318561[26]	M8β[26]	2213 ± 102
5203361404618057984	9 45 14	−77 53 14.0	15.4 ± 0.1	2MASS J09451445 − 7753150[6]	M8.2β[6]	2425 ± 20
6407490636060550400	22 35 36	−59 06 32.0	21.3 ± 0.2	2MASS J22353560 − 5906306[5]	M8.6β[6]	2289 ± 80
1349492949336359936	17 50 13	+ 44 24 06.7	32.5 ± 0.3	LSPM J1750 + 4424[27]	M8β[28]	2525 ± 26
6468916639853825664	20 28 22	−56 37 03.5	15.2 ± 0.2	2MASS J20282203 − 5637024[5]	M8γ[6]	2417 ± 41
553593388644803968	5 38 17	+ 79 31 05.4	43.1 ± 0.0	LP 16 − 36[29]	sdM[29]	2671 ± 10
6568517687360642816	22 22 56	−44 46 22.5	21.3 ± 0.3	SIPS J2222 − 4446[16]	M8β[15]	2383 ± 59
6551233295852532096	23 36 07	−35 41 50.5	21.7 ± 0.5	SIPS J2336 − 3541[16]	M8.6γ[6]	2268 ± 66
5401822669314874240	11 02 10	−34 30 35.8	16.9 ± 0.1	TWA 28[30]	M8.5γ[31]	2382 ± 42
2861861847492765568	0 08 28	+ 31 25 58.0	11.4 ± 0.6	2MASS J00082822 + 3125581[26]	M8γ[26]	2292 ± 203
5657734928392398976	9 38 40	−27 48 21.2	35.3 ± 0.1	SIPS J0938 − 2748[16]	M8β[15]	2476 ± 11
656167618671591424	8 19 46	+ 16 58 53.3	33.0 ± 0.3	2MASS J08194602 + 1658539[32]	M8β[18]	2350 ± 43
5432903251692290944	9 39 59	−38 17 18.1	16.4 ± 0.3	2MASS J09395909 − 3817217[15]	M8γ[15]	2406 ± 34
147614422487144960	4 36 33	+ 24 21 39.4	6.3 ± 0.1	2MASS J04363248 + 2421395[1]	M8γ[2]	2457 ± 11
3313381382679891456	4 32 51	+ 17 30 08.9	6.9 ± 0.4	2MASS J04325119 + 1730092[33]	M8γ[34]	2373 ± 67
1952664279346269056	21 40 39	+ 36 55 55.3	9.9 ± 0.4	2MASS J21403907 + 3655563[15]	M8β[15]	2517 ± 42
3459372646830687104	12 07 33	−39 32 54.4	15.5 ± 0.1	TWA 27[35]	M8β[36]	2430 ± 13
3459725624422311424	12 03 59	−38 21 40.6	12.2 ± 0.2	TWA 38[5]	M8γ[31]	2455 ± 22
6281432246412503424	14 44 17	−20 19 56.9	58.1 ± 0.1	SSSPM J1444 − 2019[37]	sdM9[38]	2352 ± 10
5399990638128330752	11 06 45	−37 15 11.7	9.8 ± 0.3	2MASS J11064461 − 3715115[5]	M9.4γ[6]	2396 ± 65
2898019875782441856	6 08 53	−27 53 58.2	22.6 ± 0.2	DENIS J060852.8 − 275358[32]	M9β[25]	2359 ± 102
216704503361774080	3 45 21	+ 32 18 17.6	3.1 ± 0.1	2MASS J03452106 + 3218178[39]	M9γ[40]	2588 ± 12
6152893526035165312	12 47 44	−38 16 46.8	11.9 ± 0.3	2MASS J12474428 − 3816464[41]	M9[6]	2380 ± 98
6236753694496012544	15 47 47	−24 23 51.7	29.3 ± 0.3	DENIS J154747.2 − 242349[23]	L0β[36]	2273 ± 74
6358389917097619968	21 54 49	−74 59 14.9	21.3 ± 0.2	2MASS J21544859 − 7459134[5]	M9.8γ[6]	2325 ± 32
6366726276822544768	20 00 49	−75 23 08.8	34.0 ± 0.1	SIPS J2000 − 7523[42]	M9γ[43]	2338 ± 32
365582359196918656	0 41 22	+ 35 47 12.5	9.3 ± 1.1	2MASS J00412179 + 3547133[17]	sdM9[44]	2194 ± 145
2969695320811729280	5 26 43	−18 24 31.9	18.6 ± 0.1	2MASS J05264316 − 1824315[5]	M6.2γ[6]	2663 ± 12
6845967936118138752	20 13 52	−28 06 03.3	21.0 ± 0.3	2MASS J20135152 − 2806020[23]	L0β[36]	2277 ± 68
3230008650057256960	4 43 38	+ 0 02 03.4	47.6 ± 0.1	2MASSI J0443376 + 000205[45]	M9β[46]	2290 ± 35
6096164227899898880	14 11 42	−45 24 20.1	19.1 ± 0.2	2MASS J14114474 − 4524153[47]	sdM9[48]	2487 ± 47
3478519134297202560	11 39 51	−31 59 21.8	21.4 ± 0.2	TWA 26[35]	M9γ[35]	2390 ± 17
1320853355787534848	15 52 59	+ 29 48 47.5	48.9 ± 0.2	2MASS J15525906 + 2948485[49]	L0γ[50]	2097 ± 49

Table A1 – *continued*

Gaia DR3 Source ID	α ($^{\mathrm{h\,m\,s}}$)	δ ($^{\mathrm{d\,m\,s}}$)	ϖ (mas)	Object name	Spectral type	T_{eff} (K)
6132672029732817024	12 45 14	−44 29 08.1	12.2 ± 0.3	TWA 29[51]	L0γ[36]	2317 ± 41
1458522725665649536	13 47 50	+ 33 36 01.5	13.0 ± 0.7	2MASS J13474972 + 3336019[52]	sdL0[53]	2387 ± 70
4568719543555702272	17 11 13	+ 23 26 32.5	30.9 ± 0.3	2MASSI J1711135 + 232633[46]	L1γ[36]	2065 ± 90
2328674716056981888	23 22 47	−31 33 32.1	50.2 ± 0.2	2MASS J23224684 − 3133231[23]	L0γ[23]	2017 ± 46
144711230753602048	4 35 36	+ 21 15 03.6	16.7 ± 0.6	2MASS J04353511 + 2115201[47]	sdL0[54]	2371 ± 74
5183457632811832960	3 06 02	−3 31 06.1	24.7 ± 0.3	2MASS J03060140 − 0330438[47]	sdL0[54]	2348 ± 55
4954323704550180352	1 41 58	−46 33 58.1	27.3 ± 0.4	2MASS J01415823 − 4633574[55]	L0 γ[25]	2146 ± 153
4980384088633481216	0 32 56	−44 05 07.3	29.0 ± 0.4	EROS−MP J0032 − 4405[56]	L0 γ[50]	2092 ± 83
4841448081361281920	3 57 27	−44 17 30.5	21.3 ± 0.3	2MASS J03572695 − 4417305[57]	L0 β[25]	2213 ± 115
2358397882610264960	1 16 39	−16 54 20.1	16.1 ± 0.5	2MASS J01163865 − 1654210[58]	sdL0[53]	2291 ± 96
2802623115925093760	0 43 26	+ 22 21 21.9	15.0 ± 0.3	2MASS J00432610 + 2221295[47]	sdL1[54]	2410 ± 36
4584405146372926720	17 56 10	+ 28 15 16.8	28.9 ± 0.3	2MASS J17561080 + 2815238[15]	sdL1[15]	2032 ± 108
1047188004010109440	10 22 47	+ 58 25 33.6	54.0 ± 0.2	2MASS J10224821 + 5825453[59]	L1γ[25]	2028 ± 68
1060313492785021312	11 08 30	+ 68 30 13.5	61.8 ± 0.1	LSPM J1108 + 6830[27]	L1γ[6]	2019 ± 55
2955015805492793088	5 18 46	−27 56 45.8	18.3 ± 0.6	2MASSI J0518461 − 275645[46]	L1β[46]	2183 ± 164
2781513733917711616	0 45 22	+ 16 34 44.0	65.4 ± 0.2	2MASS J00452143 + 1634446[60]	L2 β[50]	2018 ± 39
824017070904063488	10 04 20	+ 50 22 56.1	46.2 ± 0.5	G 196 − 3B[61]	L3γ[25]	1899 ± 100
3303349202364648320	3 55 24	+ 11 33 33.7	109.1 ± 0.5	2MASS J03552337 + 1133437[62]	L5 γ[50]	1839 ± 140

References. 1. Esplin, Luhman & Mamajek (2014), 2. Luhman et al. (2017), 3. Lépine, Rich & Shara (2003), 4. Reiners & Basri (2006), 5. Gagné et al. (2015b), 6. Gagné et al. (2015a), 7. Gliese & Jahreiß (1991), 8. Faherty et al. (2012), 9. Luhman et al. (2018), 10. Rebull et al. (2010), 11. Schneider et al. (2011), 12. Aganze et al. (2016), 13. Ardila, Martín & Basri (2000), 14. Tinney (1993), 15. Kirkpatrick et al. (2010), 16. Deacon & Hambly (2007), 17. Burgasser et al. (2004), 18. Bardalez Gagliuffi et al. (2014), 19. Andrei et al. (2011), 20. Marocco et al. (2013), 21. Lépine et al. (2002b), 22. Magazzù et al. (2003), 23. Reid et al. (2008), 24. Phan-Bao et al. (2003), 25. Kirkpatrick et al. (2008), 26. Kellogg et al. (2017), 27. Gizis et al. (2000), 28. Dupuy & Liu (2012), 29. Liebert et al. (1979), 30. Scholz et al. (2005), 31. Gagné et al. (2017), 32. Cruz et al. (2003), 33. Leggett & Hawkins (1989), 34. Luhman et al. (2009), 35. Gizis (2002), 36. Allers & Liu (2013), 37. Scholz et al. (2004), 38. Winters et al. (2015), 39. Cieza & Baliber (2006), 40. Luhman, Esplin & Loutrel (2016), 41. Gagné et al. (2014), 42. Ménard, Delfosse & Monin (2002), 43. Gálvez-Ortiz et al. (2014), 44. Burgasser (2004), 45. Hawley et al. (2002), 46. Cruz et al. (2007), 47. Luhman (2014a), 48. Kirkpatrick et al. (2016), 49. Wilson et al. (2003), 50. Cruz et al. (2009), 51. Looper et al. (2007), 52. West et al. (2008), 53. Zhang et al. (2017a), 54. Kirkpatrick et al. (2014), 55. Kirkpatrick et al. (2006), 56. EROS Collaboration et al. (1999), 57. Bouy et al. (2003), 58. Schneider et al. (2016), 59. Schmidt et al. (2007), 60. Salim et al. (2003), 61. Hellemans (1998), 62. Reid et al. (2006).

Note. Astrometry is from Gaia DR3 and the T_{eff} values are those produced by the ESP-UCD Apsis module and published as part of the Data Release.

This paper has been typeset from a TEX/LATEX file prepared by the author.